Time Integration of Reacting Flows and Energy-Stable Hybrid Spatial Discretizations

Cory Mikida

Department of Aerospace Engineering

University of Illinois at Urbana-Champaign

February 8, 2021

Contents

1 Time Integration of Reacting Flows

1.1 Motivation & Background

In the simulation of reacting flows, the compressible Navier–Stokes equations are augmented to include equations governing the rate of change of the mass fraction of each species in the chemical mechanism at hand based on momentum, mass diffusion, and reaction kinetics. What results is a set of equations that can feature both a wide range of timescales and a number of comparatively stiff terms that can have an adverse effect on maximum allowable timestep size and, as a byproduct, simulation performance and fidelity. In particular, the timescales of the chemical reactions are often multiple orders of magnitude lower than those of the fluid motion in practice. One approach to effectively time-marching these problems at the fluid-relevant timescale, then, is to introduce an operator-splitting technique [23, 25, 29, 40, 41, 43] in which the advection and diffusion terms in the right-hand-sides are advanced explicitly, with the chemical source term(s) being advanced implicitly and in a separate substep, typically by software packages such as CVODE [8]. However, this approach results in a scheme that is typically at best first- or second- order accurate in time globally.

To more accurately handle such situations, implicit-explicit (IMEX) time integration schemes have been developed in order to partition the governing equations and treat the stiff terms implicitly while treating the nonstiff terms explicitly. In 2003, Kennedy and Carpenter [19] introduced additive Runge–Kutta schemes for convection-diffusion-reaction equations, demonstrating a higher order of temporal accuracy than the operator splitting approach is capable of attaining. In 2011, Svärd and Mishra [45] also introduced more simplistic one-step IMEX schemes mimicking single stages in these additive-RK schemes, applying them to the reactive Euler equations and demonstrating first order with a need for numerical diffusion as the problem becomes less stiff.

Another approach to handling stiffness, and in particular the resulting disparity in timescales between different simulation components, is the use of multi-rate time integration. Gear and Wells [15] were the initial authors of work on multi-step multi-rate methods, with similar contributions provided more recently by Constantinescu and Sandu [9] for hyperbolic conservation laws. Constantinescu and Sandu later extended this work to develop implicit multi-rate schemes [10,11], but failed to introduce a scheme featuring both implicitly and explicitly advanced components within a multi-rate framework. Klöckner [22] also conducted an empirical investigation into the effects of the various design choices present in an explicit two-component scheme based on the work of Gear and Wells, with Mikida et al. [34] applying this framework to fluid simulation on overset grids using provably stable interpolation to form the coupling between grid-determined timescales.

The primary goal of this section of the thesis is production of a novel time integration scheme driving a demonstrative reacting flow problem with improved efficacy identified by superior accuracy and stability and/or faster performance relative to existing methods. The integration project being undertaken aims to augment the capabilities of the multi-rate integrators developed in [34], adding the ability to treat certain right-hand side components

implicitly as well as adapt either the macro-timestep or the step ratio of the scheme based on local truncation error estimates. These additions are explicitly designed to handle the stiffness introduced to the flow problems to which these integrators were originally applied via the introduction of chemical source terms, as well as to efficiently integrate reacting flow simulations in which the stiffness varies in time. This latter phenomenon is especially common in ignition simulations, where the high-stiffness qualities of the kinetics during ignition contrast with surrounding simulation time in which the mass fractions are at or near chemical equilibrium.

A critical component in our effort will be comparison of the resulting scheme with CVODE as a proxy for the state of the art in time integration of chemically reacting flows, with the goal of achieving superiority in terms of observed temporal accuracy of the entire system (initially targeting improvement over the low-order operator splitting approach), or in terms of performance (most accurately measurable by a reduction in the number of chemistry right-hand-side evaluations required to reach a given solution time).

Meanwhile, an aspect of the algorithms being implemented that has been identified early as beyond our bounds is the presence of multi-variable solves in a number of potential adaptive implicit integration scenarios, namely:

- Coupled implicit right-hand-sides

- Use of adaptive timestep controllers where the local error estimate of all solution components makes use of implicit and explicit state estimates.

With these goals and bounds in mind, the proposed thesis has the potential to have a significant impact on the simulation of reacting flows, of which there are countless real-world applications including (but not limited to) subsonic and supersonic combustion for propulsion (gas turbines, ramjets/scramjets, rockets), energy efficiency of furnaces and residential heating, and solution of problems relating to atmospheric and climate sciences.

1.2 Governing Equations

The problem at hand involves the simulation of chemically reacting flows, the governing equations of which amount to the Navier–Stokes equations with (in our form)

- The addition of a governing equation for the rate of change of the mass fractions of each species in the chemical mechanism simulated

- The addition of governing equations specifying the rate of change of temperature and pressure, derived from an assumption of constant internal energy and volume in a reaction substep (for the former) and the ideal gas law (for the latter).

These equations are given below, along with a brief explanation of the notation/nomenclature used.

$$\frac{\partial \rho}{\partial t} + \frac{\partial}{\partial x_j}(\rho u_j) = 0 \tag{1}$$

$$\frac{\partial}{\partial t}(\rho u_i) + \frac{\partial}{\partial x_j}(\rho u_i u_j + P\delta_{ij} - \tau_{ij}) = 0 \tag{2}$$

$$\frac{\partial}{\partial t}(\rho E) + \frac{\partial}{\partial x_j}((\rho E + P)u_j + q_j - u_i\tau_{ij}) = 0 \tag{3}$$

$$\frac{\partial}{\partial t}(\rho Y_k) + \frac{\partial}{\partial x_j}(\rho Y_k u_j - \varphi_{ki}) = W_k\dot{\omega}_k \tag{4}$$

$$\frac{\partial T}{\partial t} + \frac{\sum_{k=1}^{N_{sp}} U_k(T)\frac{\partial \rho Y_k}{\partial t}\frac{1}{W_k}}{\sum_{k=1}^{N_{sp}}[C]_k C_{v,k}(T)} = 0 \tag{5}$$

$$\frac{\partial P}{\partial t} - \frac{R}{V}(T\frac{\partial n}{\partial t} + \frac{\partial T}{\partial t}n) = 0 \tag{6}$$

In these equations, ρ is the fluid density, u_i is the velocity in the i-th direction, and E is the total energy density, calculated as

$$E = U + \frac{1}{2}\sum u_i^2 \tag{7}$$

where U is the total internal energy of the gas mixture. δ_{ij} is the Kronecker delta, P is the pressure, T is the temperature, R is the universal gas constant, and Y_k is the mass fraction of species k. $[C]_k$ is the concentration of species k in the gas mixture, N_{sp} is the number of species in the chemical mechanism, W_k is the molecular weight of species k, n is the number of moles of the gas mixture, V is the volume of the gas, and $\dot{\omega}_k$ is the net production rate of species k. τ_{ij} is the viscous stress tensor, φ_{ki} are the diffusion fluxes, and q_j are the heat fluxes, defined by

$$q_j = -\frac{\partial(\lambda T)}{\partial x_j} + h_k\varphi_{kj}. \tag{8}$$

In this expression, λ is the thermal conductivity, and h_k is the enthalpy of species k. $C_{v,k}(T)$ is the specific heat at constant volume of species k at temperature T, and $U_k(T)$ is the internal energy of species k at temperature T. These quantities are defined using the NASA 9-coefficient polynomial parameterization [32], such that

$$\frac{C_{v,k}(T)}{R} = a_0 + a_1 T + a_2 T^2 + a_3 T^3 + a_4 T^4 - 1 \tag{9}$$

$$\frac{U_k(T)}{RT} = a_0 + \frac{a_1}{2}T + \frac{a_2}{3}T^2 + \frac{a_3}{4}T^3 + \frac{a_4}{5}T^4 + \frac{a_5}{T} - 1, \tag{10}$$

where the a coefficients are defined per-species for an arbitrary number of temperature regions.

As for the diffusion fluxes, these are defined using a mixture-averaged approach — that is, φ_{ki} is given by

$$\varphi_{ki} = \varphi_{ki}^* + \varphi_{ki}^c, \tag{11}$$

where φ_{ki}^* is the mixture-averaged approximation, and φ_{ki}^c is a correction term to ensure mass conservation. The mixture-averaged approximation is defined by

$$\varphi_{ki}^* = -\rho D_{k,m} \frac{W_k}{W} \frac{\partial X_k}{\partial x_i}, \tag{12}$$

where $D_{k,m}$ is the mixture-averaged diffusivity of species k, W is the mean molecular weight, and X_k is the mole fraction of species k. Finally, the correction term is given by

$$\varphi_{ki}^c = -Y_k \sum_{n=1}^{N_{sp}} \varphi_{ni}^*. \tag{13}$$

1.3 Numerical Methods

1.3.1 Adams Methods

For clarity, here we provide a brief derivation of a standard Adams–Bashforth (AB) integrator, as described in [3], starting from a model initial value problem (IVP) given by

$$\frac{\mathrm{d}y}{\mathrm{d}t} = F(t, y), \quad y(0) = y_0. \tag{14}$$

Applying a method of lines (MOL) approach to spatially discretize and solve the reactive Navier–Stokes equations (1)–(6) ultimately provides this form. We approximate the time dependency of the right-hand side function with a polynomial with coefficients $\boldsymbol{\alpha}$ (formed by interpolating past values of $F(t, y)$), extrapolate with that polynomial approximation, and integrate the extrapolant. To obtain the coefficients $\boldsymbol{\alpha}$ used to form this history-interpolating polynomial, we construct a linear system using a Vandermonde matrix:

$$V^T \cdot \boldsymbol{\alpha} = \int_0^{\Delta t} \tau^i d\tau = \frac{(\Delta t)^i}{i+1}, \quad i = 1, 2..., n, \quad V = \begin{bmatrix} 1 & t_1 & \dots & t_1^{n-1} \\ 1 & t_2 & \dots & t_2^{n-1} \\ \vdots & \vdots & \ddots & \vdots \\ 1 & t_n & \dots & t_n^{n-1} \end{bmatrix}, \tag{15}$$

where $\int_0^{\Delta t} \tau^i d\tau$ is a vector evaluating the integral of the interpolation polynomial, and V is the Vandermonde matrix with monomial basis and nodes $t_1, t_2, \dots t_n$, corresponding to past time values. In Eqn. (15), n is equal to the order of the integrator, and t_i are the time history values, with $0 \le t_1 < t_2 \dots < t_n$. The coefficients $\boldsymbol{\alpha}$ are used to extrapolate to the next state via

$$\begin{aligned} y(t_{i+1}) = y(t_i) &+ \alpha_1 F(t_{i-n}, y_{i-n}) + \alpha_2 F(t_{i-n-1}, y_{i-n-1}) \\ &+ \cdots + \alpha_n F(t_i, y_i). \end{aligned} \tag{16}$$

1.3.2 Multi-rate Adams Methods

We now describe a multi-rate generalization of the scheme, making use of the algorithm introduced in [15]. We consider the following model system with "fast" and "slow" solution

components:

$$\frac{\mathrm{d}}{\mathrm{d}t} \left(\begin{array}{c} f(t) \\ s(t) \end{array} \right) = \left(\begin{array}{c} a_f(f, s) \\ a_s(f, s) \end{array} \right).$$ (17)

With this in mind, we can set a slow (larger) time step H for a_s such that we maintain stability in the integration of the slow component. We also set a fast time step h for a_f such that H is an integer multiple of h, and define the ratio between the two, $SR = H/h$, as the step ratio of the multi-rate scheme. While the reactive flow scheme presented here makes use of only two separate state components, each with its own right-hand side function and independent rate, the theory is readily extensible to any number of rates.

Within this two-component scheme, a few design choices are available:

- The order in which we evaluate and advance the solution components. Namely, two primary options are advancing the fast-evolving solution component through all of its micro-timesteps h and waiting to perform the single macro-timestep H required for the slow component until the end (a "fastest-first" scheme, per the nomenclature of [15]), or pursuing an algorithm in which the slow component is instead advanced first.

- For slowest-first evaluation schemes, the choice of whether or not to re-extrapolate the slow state after additional state and right-hand side information is gathered at the micro-timestep level.

Empirical observations on the effects of these choices are made in [22], with a step-by-step walkthrough of the evaluations present in a single macrostep of a fastest-first scheme given by [34]. The code implementing this method, as well as other methods within the multi-rate Adams framework, is generated by the Python packages Leap [21] and Dagrt [20], and all time integration scheme development is occurring via implementation in Leap.

To fully realize the potential multi-rate formulation for reacting Navier–Stokes problems (for which the matrix of right-hand sides is not as simple as in [34], where both right-hand sides and state components are realized as per-overset-grid quantities), we need to introduce additive terms to Eqn. (17), which we express as terms coupling the fast and slow states (a_{fs} and a_{sf}) and self-influencing terms (a_{ff} and a_{ss}):

$$\frac{\mathrm{d}}{\mathrm{d}t} \left(\begin{array}{c} f(t) \\ s(t) \end{array} \right) = \left(\begin{array}{c} a_{ff}(f, s) + a_{fs}(f, s) \\ a_{sf}(f, s) + a_{ss}(f, s) \end{array} \right).$$ (18)

In the reacting flow formulation with which we are concerned (Eqn. (1)–(6)), we define the "fast" component of our Navier–Stokes solution as a vector of the mass fractions of the species as well as the temperature and pressure, $[\rho Y_k, T, P]^T$. The "slow" component is then defined as the set of typical conserved variables in a non-reacting simulation, $[\rho, (\rho \vec{u}), (\rho E)]^T$. As a result, one possible definition of the additive terms in Eqn. (18) can

be given as follows:

$$a_{ff}(f, s) = \begin{pmatrix} W_k \dot{\omega}_k \\ -\dfrac{\sum_{k=1}^{N_{sp}} U_k(T) \frac{\partial \rho Y_k}{\partial t} \frac{1}{W_k}}{\sum_{k=1}^{N_{sp}} [C]_k C_{v,k}(T)} \\ \dfrac{R}{V} \left(T \frac{\partial n}{\partial t} + \frac{\partial T}{\partial t} n \right) \end{pmatrix}$$

$$a_{fs}(f, s) = \begin{pmatrix} -\frac{\partial}{\partial x_j} \left(\rho Y_k u_j - \varphi_{ki} \right) \\ 0 \\ 0 \end{pmatrix}$$

$$a_{sf}(f, s) = \begin{pmatrix} 0 \\ -\frac{\partial}{\partial x_j} \left(P \delta_{ij} \right) \\ -\frac{\partial}{\partial x_j} \left(P u_j \right) \end{pmatrix}$$

$$a_{ss}(f, s) = \begin{pmatrix} -\frac{\partial}{\partial x_j} \left(\rho u_j \right) \\ -\frac{\partial}{\partial x_j} \left(\rho u_i u_j - \tau_{ij} \right) \\ -\frac{\partial}{\partial x_j} \left((\rho E) u_j + q_j - u_i \tau_{ij} \right) \end{pmatrix}$$

As our treatment of this set of equations with multi-rate integration develops, so too will our approach to defining the additive terms of Eqn. (18), as well as which state variables are deserving of fast or slow treatment.

1.3.3 Implicit Adams Methods and Extension to Multi-rate

The concepts in the previous sections, both single- and multi-rate, are easily extended to include implicit integration methods. We define an implicit Adams (Adams–Moulton [35]) method in the same manner as above, starting with the same simplified IVP of Eqn. (14) and expressing the scheme as

$$y(t_{i+1}) = y(t_i) + \beta_1 F(t_{i-n+1}, y_{i-n+1}) + \beta_2 F(t_{i-n}, y_{i-n}) + \cdots + \beta_n F(t_{i+1}, y_{i+1}). \tag{19}$$

The coefficients $\boldsymbol{\beta}$ are constructed in a manner identical to the Adams-Bashforth coefficients $\boldsymbol{\alpha}$ (see Eqn. (15)), using temporal nodes shifted by Δt forward in time.

Extension of this implicit method into the multi-rate framework is straightforward, given that the driving principle of the Adams–Moulton method (namely, maintenance of right-hand side history values through which to extrapolate) is the same as that of Adams–Bashforth, and amounts to allowing the histories of each right-hand side term to maintain their own timestep intervals.

In the case that implicit time integration is used, it will be used to drive $a_{ff}(f, s)$. In order to perform the implicit solve required to advance this right-hand side via Adams–Moulton (see Eqn. (19)), a Jacobian matrix is required. While other implementations such as CVODE's adaptive backward differentiation formula (BDF) algorithm for stiff problems

often make use of finite-difference generated Jacobians, we will instead use PyJac-V2 [12] to obtain the analytical Jacobian for a given chemical mechanism via code generation, which will then be used by a simple Newton algorithm to perform the implicit solve. More details on the construction of this Jacobian are given by Curtis et al. [12], but we document the basic form, in addition to an alternate differential-algebraic formulation, below.

The chemical kinetics Jacobian can be written as the matrix

$$J = \frac{\partial f_i}{\partial \Phi_j}, \tag{20}$$

where f is the set of right-hand sides directly pertaining to the kinetics and reactive source term:

$$f = \left(\frac{dT}{dt}, \frac{dP}{dt}, \frac{dn_1}{dt}, \frac{dn_2}{dt}, \ldots \frac{dn_{N_{sp}-1}}{dt} \right). \tag{21}$$

Here, n_i is the number of moles of species i in the mixture. While the temperature and pressure right-hand sides are given by Eqn. (5) and (6), note that the molar source terms pertain only to the net production rates of the species:

$$\frac{dn_i}{dt} = V \dot{\omega}_i. \tag{22}$$

Note also (based on the structure of PyJac-V2) that the state vector for the Jacobian is defined using the number of moles of each species in the chemical mechanism rather than the mass fractions:

$$\Phi = \left(T, P, n_1, n_2, \ldots n_{N_{sp}-1} \right). \tag{23}$$

The number of moles of the last species in the mixture is calculated via the mass fractions summing to 1.

With these definitions in mind, we can expand Eqn. (20) and express it in true matrix form:

$$J = \begin{bmatrix} \frac{d\dot{T}}{dT} & \frac{d\dot{T}}{dP} & \frac{d\dot{T}}{dn_1} & \cdots & \frac{d\dot{T}}{dn_{N_{sp}-1}} \\ \frac{d\dot{P}}{dT} & \frac{d\dot{P}}{dP} & \frac{d\dot{P}}{dn_1} & \cdots & \frac{d\dot{P}}{dn_{N_{sp}-1}} \\ \frac{d\dot{n}_1}{dT} & \frac{d\dot{n}_1}{dP} & \frac{d\dot{n}_1}{dn_1} & \cdots & \frac{d\dot{n}_1}{dn_{N_{sp}-1}} \\ \vdots & \vdots & \vdots & \ddots & \vdots \\ \frac{d\dot{n}_{N_{sp}-1}}{dT} & \frac{d\dot{n}_{N_{sp}-1}}{dP} & \frac{d\dot{n}_{N_{sp}-1}}{dn_1} & \cdots & \frac{d\dot{n}_{N_{sp}-1}}{dn_{N_{sp}-1}} \end{bmatrix}. \tag{24}$$

Providing this matrix to the implicit solver should serve to reduce the number of chemical right-hand side calls required to time-march the system relative to methods that employ a finite-difference generated Jacobian, which will directly improve performance.

A critical consideration in the formulation of both the governing equations and the chemical Jacobian will be maintaining a solution that lies on the ideal gas constraint manifold. This has been identified in early work as a potential concern when fully differential approaches
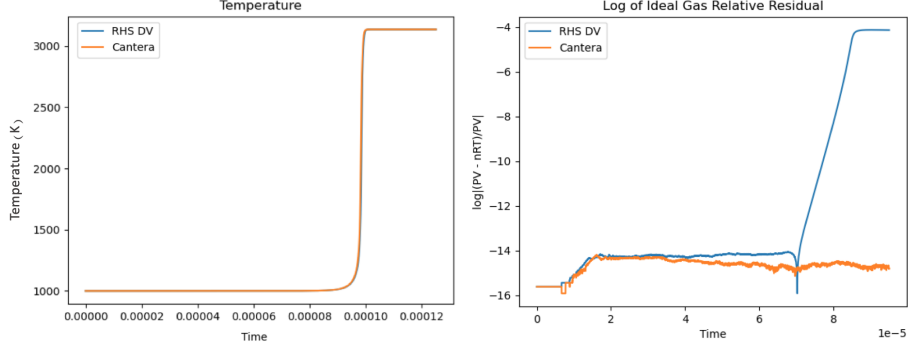
Figure 1: Temperature profiles (left) and relative ideal gas law residual (right) for advancement of homogeneous H2-O2 autoignition example (employing the nine-species San Diego mechanism [48]) using a fully differential approach (blue) versus a differential-algebraic approach (orange) where the constant internal energy and ideal gas law constraints are fulfilled by a Newton solve within Cantera [16].

to solving the governing equations that time-march the rates-of-change of temperature and pressure (as opposed to differential-algebraic approaches that directly satisfy the ideal gas and constant internal energy constraints) are used (see Figure 1). To avoid drift off of the ideal gas law manifold, a chemical kinetic Jacobian modified to include the algebraic constraints explicitly can be used. This approach, detailed in Hung [18], modifies the molar source terms to incorporate this constraint while removing the temperature and pressure source terms (which we then replace with a temperature Newton solve based on the constant internal energy constraint via Cantera [16], as well as a direct application of the ideal gas law to obtain the pressure). This modified Jacobian can be expressed as

$$J^* = \begin{bmatrix} \frac{d\dot{n}_1^*}{dn_1} & \cdots & \frac{d\dot{n}_1^*}{dn_{N_{sp}-1}} \\ \vdots & \ddots & \vdots \\ \frac{d\dot{n}_{N_{sp}-1}^*}{dn_1} & \cdots & \frac{d\dot{n}_{N_{sp}-1}^*}{dn_{N_{sp}-1}} \end{bmatrix} \tag{25}$$

where

$$\frac{d\dot{n}_i^*}{dn_j} = \frac{d\dot{n}_i}{dn_j} - \frac{U_j}{C_v}\frac{d\dot{n}_i}{dT}. \tag{26}$$

In this expression, U_j is the contribution of the j-th species to the internal energy, and C_v is the specific heat of the mixture at constant volume.

Which of these Jacobians is ideal for our purposes is a consideration worth monitoring as our implicit integration techniques develop, but for now we employ the differential-algebraic approach of Eqn. (25). Additionally, a third relatively unexplored approach would use the fully differential method with pressure and temperature source terms, while also using penalization to force the solution towards the constraint manifold. This attenuation approach is described in some detail (albeit for smaller model problems) by Ascher and Petzold [2].

1.3.4 Timestep Control Algorithm

Early implicit-explicit runs of small-scale reacting flow problems quickly identified a need to adapt the timestep of the integrator based on relative and/or absolute local error demands. We therefore employ a timestep control algorithm which, in its current form, is similar to that of CVODE, using a weighted root-mean-square norm to more adequately handle states with components that feature a large variation in magnitude. The weights are calculated as

$$w_i = \frac{1}{\text{ATOL} + \text{RTOL}|s_{q,i}|} \tag{27}$$

with the weighted root-mean-square norm then being given by

$$\|E\|_{wrms} = \left(\sum_{i=1}^{N} \frac{1}{N}(w_i(s_{q+1,i} - s_{q,i}))^2\right)^{1/2}, \tag{28}$$

where $s_{q,i}$ is the i-th component of the state estimate obtained using an order-q scheme. The timestep is *decreased* if $\|E\|_{wrms} \geq 1$ via

$$\Delta t = 0.9\Delta t(\|E\|_{wrms})^{-1/q} \tag{29}$$

and *increased* if $\|E\|_{wrms} < 1$ via

$$\Delta t = 0.9\Delta t(\|E\|_{wrms})^{-1/(q+1)}. \tag{30}$$

This added capability presents a number of questions in terms of how best to accomplish this error control. In particular, step ratio adjustment *in situ*, rather than timestep adjustment, to meet error needs provides an implementation challenge in terms of code generation of these integrators, whereas the choice of which solution component(s) are involved in error estimation/timestep control also presents a design decision that could have notable effect on numerical performance.

1.4 Validation Plan

The efficacy of the time integrators constructed via the above methodology will be assessed using a reacting mixing layer problem with a hyperbolic tangent velocity profile for the baseflow (as used by [33] and [4]), with the San Diego 9-species chemical mechanism [48] employed for the chemical kinetics. By perturbing this baseflow with the mode having the highest growth rate to instability (reproduced based on the inviscid analyses of [33] and [4]), and by varying the temperature in the domain to induce ignition local to the mixing layer, we can establish a fast-evolving solution component (the chemical kinetics of the ignition) and a slow-evolving solution component (the fluid motion), both possessing accessible means of rate modification (for the chemistry, we can accomplish this by scaling the pre-exponential factors in the Arrhenius reaction rates, and for the fluid, we can scale the magnitude of the initial crossflow velocity). In doing so, what should result is a problem with ample testbed capabilities for our new multi-rate integrators, and also a problem firmly rooted in physical utility in that it provides the simplest model for scramjet/ramjet combustion processes.
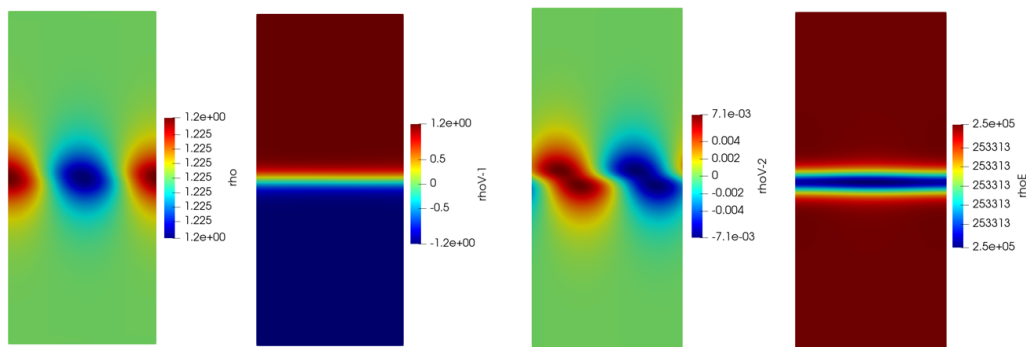
Figure 2: Perturbed initial condition of the hyperbolic tangent example using sea-level air.
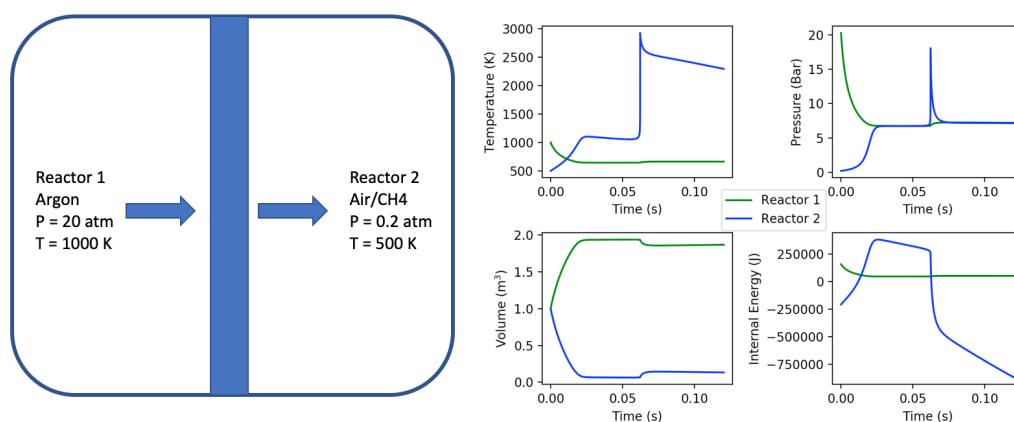

Figure 3: Cantera two-reactor example problem. The solution shown is obtained using Cantera's internal reactor system integrator, which is based on the same BDF algorithm employed by CVODE. The piston velocity is initially zero, with ignition eventually occuring in the air-methane reactor.

1.5 Outlook

1.5.1 Current Status

At present, implicit-explicit time integration of reacting flows using Runge–Kutta based methods in conjunction with code generation of source terms and Jacobians for the chemical mechanisms is implemented and undergoing testing with the fluid solver application. Implicit Adams methods (with single-rate Adams–Moulton being the baseline) for the purposes of chemistry integration are also being implemented, along with an application of the error-informed timestep control algorithm to both single-rate and multi-rate Adams methods. Construction of implicit-explicit multi-rate Adams methods with error-informed adaptivity are well underway, with testing of fully-explicit adaptive Adams multi-rate integrators on a stiff small-scale Cantera [16] two-reactor system in progress. A schematic of this problem, which is based in large part on an example problem bundled with the software, is given in Figure 3. While the governing equations for this problem are not the same as those generated by PyJac-V2, our hope is that it will serve as a suitably small stiff

test problem to be used as a stepping stone in verification of the error-informed timestep controller for explicit methods, as well as further exploration of its efficacy.

As for the reacting crossflow validation problem, an initial setup employing cold flow (no autoignition) with the perturbed baseflow applied to sea level air is complete (see Figure 2), with validation via the growth rate of the unstable mode completed. Also implemented in the reacting flow solver is a one-dimensional laminar free flame problem, which may also be used as a first-pass validation (via comparison to the Cantera-estimated steady-state flame speed) for new integration methods for reacting flows as they become available. A basic description of this case, as well as flame speed data generated via a Leap-generated IMEX additive Runge–Kutta integrator using PyJac-V2 analytical Jacobians, is given in the next section.

1.5.2 Risk Mitigation

Assuming demonstration of improved performance and/or accuracy of the *multi-rate* integrators over the state-of-the-art is for reasons unforseen impossible, a "fallback" takeaway would be demonstration of improvement over a low-order splitting approach via Leap implementation of an existing IMEX Runge–Kutta based scheme [19] that treats the chemistry implicitly via code-generated analytical Jacobians. Given the use of a coupled implicit-explicit scheme (for which high order has already been proven in other circumstances), as well as a chemical Jacobian that is more accurately and efficiently obtained than via finite differences (the method of CVODE), this outcome should be attainable at minimum.

As a step towards proving this, we have implemented a small-scale one-dimensional free-flame test, wherein we use a code-generated implementation of the fourth-order additive Runge-Kutta scheme of Kennedy and Carpenter to drive a simulation of a premixed, freely propagating hydrogen flame with an unburned gas temperature of 300 K at a pressure of one atmosphere (see Figure 4). Comparing the estimated laminar flame speed to that of a steady-state analysis performed by Cantera at a number of equivalence ratios ϕ, we see suitable agreement of less than 3% error, indicating that the reacting flow equations — and in particular the chemical source terms and Jacobians — are correctly implemented and ready for both further experimentation with multi-rate timescale splitting and a more thorough analysis of performance.

ϕ	Leap S_L (m/s)	Cantera S_L (m/s)	% Error
0.75	1.585566	1.599170	0.85
1.0	2.351950	2.421837	2.89
1.5	3.1734067	3.153888	0.62

Table 1: Comparing the laminar flame speeds estimated by Leap-PyJac-V2 chemistry integration and by Cantera's steady-state analysis.
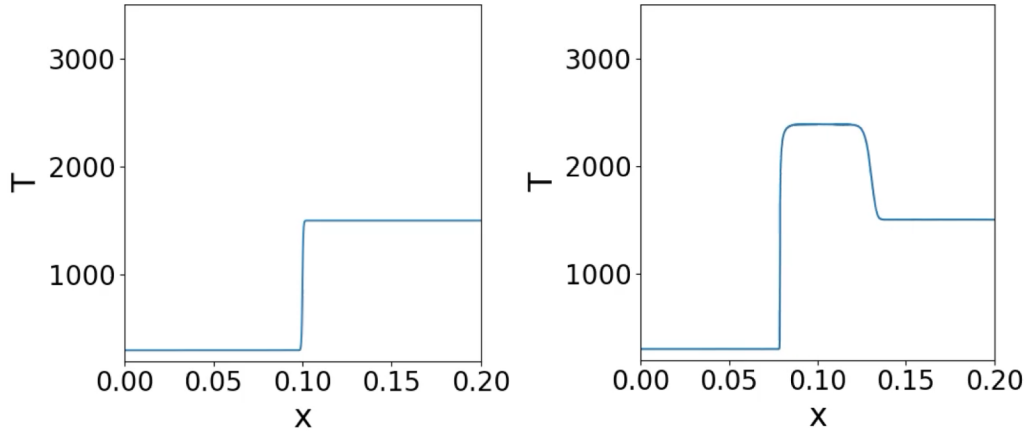
Figure 4: Figures showing the temperature profile of the one-dimensional free-flame example at initial
condition (left) and after 0.0025 seconds (right).

2 Energy-Stable Hybrid Spatial Discretizations

2.1 Motivation & Background

When simulating problems in computational fluid dynamics involving complex geometries,
numerical difficulties are often encountered that require employing one of a number of
different approaches to mitigate loss of accuracy and/or stability due to poor spatial reso-
lution. While finite-difference approaches to spatial discretization are popular due to their
simplicity and efficiency when working with smooth solutions, their geometric flexibility
is typically limited in spite of the well-documented ability to use coordinate transforms to
create intricate curvilinear meshes, as well as the ability to use overset meshes [6, 38] to
produce higher resolution in particularly troublesome sections of the spatial domain.

In particular, the summation-by-parts (SBP) methodology pioneered by Strand [42], which
mimics integration-by-parts in the discrete sense and is provably stable via the energy
method when coupled with weak enforcement of boundary conditions (simultaneous ap-
proximation term; see [44]), is an attractive method when it comes to finite differences, and
its geometric flexibility has recently been further improved by a large body of work in cre-
ating accurate and stable interfaces between nonconforming blocks. In 2010, Mattsson and
Carpenter [30] introduced interpolation operators that maintained the stability and high-
order accuracy of the underlying spatial scheme on each block, but the resulting scheme
is based on a fixed refinement ratio and the requirement that the blocks conform at their
corners (the latter of these characteristics was later removed by Nissen et al. in 2015 [36]).
The use of SBP-SAT finite difference techniques in conjunction with nonconforming grid
interfaces has been further extended to use with the second-order wave equation [47], 3D
elastic wave simulations [14], the Schrödinger equations [37], and the advection-diffusion
equation [27].

Meanwhile, another attractive approach to modeling complex geometries more efficiently
with a localized spatial discretization change is to create a hybrid spatial discretization
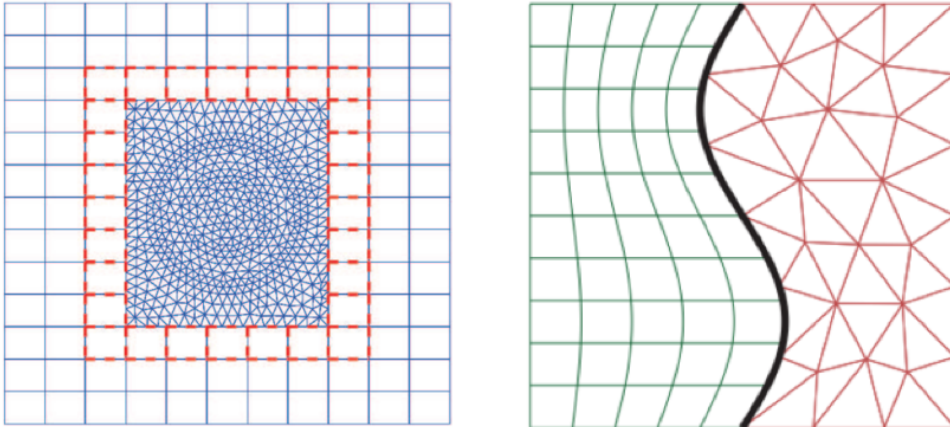
Figure 5: Two examples demonstrating the use of nonconforming interfaces. Left: Zhu, Chen, Zhong, and Liu [49]. Right: Kozdon and Wilcox [24]

that requires an interface between a high-order finite difference method (used away from the complex boundary) and an unstructured mesh with improved geometric flexibility (used near the complex boundary). Nordström and Gong proposed such a scheme in 2006 [39], coupling a high-order finite difference method and a second-order finite volume scheme. More recently, in 2016, Kozdon and Wilcox [24] developed an interface method between SBP finite-difference blocks that was based on projection into an intermediate "glue" grid characterized by piecewise polynomials, with the method also extending to the coupling of SBP finite-difference methods and discontinuous Galerkin methods. In this work, the interface method was proven to be stable via the energy method, but the projection operators were not fully determined and were based in part on an optimization procedure focused on driving the product of the projection matrices closer to an identity operation. Furthermore, the method was not extended to three dimensions, and the method is reduced to first order accuracy if the continuous coordinate transforms on either side of the interface are dissimilar. Since, Friedrich et al. [13] extended the method(s) of Kozdon and Wilcox to make the projection process degree-preserving (a characteristic that had been previously shown to be problematic by Lundquist and Nordström [28]) as well as energy-stable and conservative, but their approach still results in projection operators that are not fully determined, relying upon an optimization procedure to produce the operators that give their results. In 2019, Almquist et al. [1] developed new order-preserving interpolation operators that accomplished the same goal as Friedrich et al. without increasing the quadrature order, and which extended to problems with second-order spatial derivatives, but their results again were confined to problems with a fixed 2:1 refinement ratio. Furthermore, unlike Kozdon and Wilcox, the methods of both Almquist and Friedrich fail to extend their method to hybrid structured-unstructured discretizations.

This section of the thesis targets a lack of fully-determined high-order accurate and provably stable interface conditions between structured and unstructured meshes for computational fluid dynamic simulations. The key contribution of this work will be the construction

of an interface between structured (finite difference SBP) and unstructured (DG) spatial discretizations that does not rely upon optimization or an unequal number of constraints and unknowns for construction of the solution projections. Currently, our plan is to match the approach of [24], with the interface being defined by operators $\boldsymbol{P}_{a2b}$ and $\boldsymbol{P}_{b2a}$ that project the solution along the edge of discretization a into discretization b, and vice versa.

An additional goal to be pursued in conjunction with a unisolvent procedure while maintaining accuracy and stability is a resulting projection process that is able to provide "round-trip" fidelity of projection, meaning that projection from the structured grid to the unstructured grid and back (and vice versa) results in a solution identical to the starting point. This characteristic is one that the operators of [24] lack, even in projection from one grid into the intermediate glue layer.

The strategy for pursuance of these goals begins with consideration of the *interior* projection operator only, given the simplicity of the existing interior stencil relative to the boundary (which features many more unknowns). Noting also that the compatibility condition, which we will later find to be the critical condition for proving a stable interface, disallows us from obtaining exact "round-trip" projection, other conditions may be considered based on further manipulation or restructuring of the edge energy dissipation relations, which will be given for both structured and unstructured spatial discretizations in subsequent sections. Should a procedure for fully-determined interior interface conditions be applied successfully to a periodic problem, the boundary interface will subsequently be considered.

2.2 Governing Equations

The initial problem to which our new interface method will be targeted is the acoustic wave equation in two dimensions, in first-order form:

$$\rho\frac{\partial v_i}{\partial t} + \frac{\partial p}{\partial x_i} = 0 \ \ (i = 1, 2), \tag{31}$$

$$\frac{\partial p}{\partial t} + \lambda\left(\frac{\partial v_1}{\partial x_1} + \frac{\partial v_2}{\partial x_2}\right) = 0 \tag{32}$$

As in [24], our aim will be to prove the semi-discrete hybrid discretization stable via the energy method by proving that

$$\frac{d\mathcal{E}}{dt} \leq 0 \tag{33}$$

where the total energy of the semi-discrete system $\mathcal{E}$ is obtained by summing the energy E of each discretization block:

$$\mathcal{E} = \sum_{blocks} E. \tag{34}$$

The definitions of the energy dissipation rates for each block (each having its own spatial discretization), are given in subsequent sections.

2.3 Numerical Methods

2.3.1 Summation-by-Parts Operators

For the structured discretization that makes up one component of the proposed hybrid setup, we make use of several finite difference operators that possess the summation-by-parts (SBP) property. Taking two matrices H, Q, we here state that these two matrices are SBP matrices of order p provided

- $H^{-1}Qv$ is an order h^p approximation to $\partial/\partial x$, where h is the spatial step size in one dimension.

- H is a symmetric positive-definite matrix.

- $Q + Q^T = \text{diag}(-1, 0, 0, ..., 0, 1)$.

These conditions together ensure that the discrete version of the integration by parts property holds; that is,

$$\langle H^{-1}Qx, y \rangle_H = x_N y_N - x_1 y_1 - \langle x, H^{-1}Qy \rangle_H.$$

Note that these SBP operators do not alone guarantee strict stability for an initial boundary value problem. We must also apply the boundary conditions using a formulation that permits an energy estimate. More information on these boundary conditions, called simultaneous approximation term (SAT) boundary conditions, can be found in [5, 44, 46]. Additionally, more information on SBP operators of various orders, including the coefficients themselves, can be found in [7, 31, 42]. For this work, we will employ diagonal-norm SBP operators for the finite difference discretizations.

The SBP-SAT spatial discretization of the governing equations in the previous section (Eqn. (31)–(32)), in two dimensions and including the effect of coordinate transform from the physical space to a reference space $[-1, 1] \times [-1, 1]$, is given by

$$\rho \boldsymbol{J} \frac{d\boldsymbol{v}_i}{dt} + \boldsymbol{D}_1 \boldsymbol{J} \frac{\partial \boldsymbol{\xi_1}}{\partial \boldsymbol{x_i}} \boldsymbol{p} + \boldsymbol{D}_2 \boldsymbol{J} \frac{\partial \boldsymbol{\xi_2}}{\partial \boldsymbol{x_i}} \boldsymbol{p} = -\boldsymbol{H}^{-1} \boldsymbol{\mathcal{F}}_{v_i}, \quad i = 1, 2, \tag{35}$$

$$\boldsymbol{J} \frac{\partial \boldsymbol{p}}{\partial t} + \lambda \left(\boldsymbol{J} \frac{\partial \boldsymbol{\xi_1}}{\partial \boldsymbol{x_1}} \boldsymbol{D}_1 v_1 + \boldsymbol{J} \frac{\partial \boldsymbol{\xi_2}}{\partial \boldsymbol{x_1}} \boldsymbol{D}_2 v_1 + \boldsymbol{J} \frac{\partial \boldsymbol{\xi_1}}{\partial \boldsymbol{x_2}} \boldsymbol{D}_1 v_2 + \boldsymbol{J} \frac{\partial \boldsymbol{\xi_2}}{\partial \boldsymbol{x_2}} \boldsymbol{D}_2 v_2 \right) = -\lambda \boldsymbol{H}^{-1} \boldsymbol{\mathcal{F}}_p, \tag{36}$$

where bold letters denote matrices or vectors. Here, we have defined the matrices

$$\boldsymbol{H} = \boldsymbol{H}_{N_1} \otimes \boldsymbol{H}_{N_2}, \qquad \boldsymbol{D}_1 = \boldsymbol{D}_{N_1} \otimes \boldsymbol{I}_{N_2}, \qquad \boldsymbol{D}_2 = \boldsymbol{I}_{N_1} \otimes \boldsymbol{D}_{N_2}, \tag{37}$$

where $\boldsymbol{D}_i = \boldsymbol{H}_i^{-1} \boldsymbol{Q}_i$ defines an SBP approximation of $\frac{\partial}{\partial x_i}$. We define corresponding solution vectors as, for example,

$$\boldsymbol{p} = \begin{bmatrix} p_{00} & p_{01} & \cdots & p_{0N_2} & p_{10} & \cdots & p_{N_1 N_2} \end{bmatrix}^T \tag{38}$$

for a domain of size $(N_1 + 1) \times (N_2 + 1)$. Note also that in these equations, x_i refer to coordinates in the physical domain, whereas ξ_i refer to coordinates in the reference domain. The matrix $\boldsymbol{J}$ is a diagonal matrix

$$\boldsymbol{J} = \text{diag} \begin{bmatrix} J_{00} & J_{01} & \cdots & J_{0N_2} & J_{10} & \cdots & J_{N_1 N_2} \end{bmatrix}, \tag{39}$$

where the elements J_{kl} correspond to Jacobian determinants at grid point (k, l):

$$J = \frac{\partial x_1}{\partial \xi_1} \frac{\partial x_2}{\partial \xi_2} - \frac{\partial x_2}{\partial \xi_1} \frac{\partial x_1}{\partial \xi_2}. \tag{40}$$

The bolded coordinate transform matrices $\frac{\partial \boldsymbol{\xi_i}}{\partial \boldsymbol{x_j}}$ and $\frac{\partial \boldsymbol{x_i}}{\partial \boldsymbol{\xi_j}}$ are defined analogously.

The penalty terms in the above equations implement the boundary conditions via the SAT method, and are defined as follows:

$$\boldsymbol{\mathcal{F}}_{v_i} = \left(\boldsymbol{e}_W \otimes \boldsymbol{\mathcal{F}}_{v_i}^W\right) + \left(\boldsymbol{e}_E \otimes \boldsymbol{\mathcal{F}}_{v_i}^E\right) + \left(\boldsymbol{\mathcal{F}}_{v_i}^S \otimes \boldsymbol{e}_S\right) + \left(\boldsymbol{\mathcal{F}}_{v_i}^N \otimes \boldsymbol{e}_N\right), \tag{41}$$

$$\boldsymbol{\mathcal{F}}_p = \left(\boldsymbol{e}_W \otimes \boldsymbol{\mathcal{F}}_p^W\right) + \left(\boldsymbol{e}_E \otimes \boldsymbol{\mathcal{F}}_p^E\right) + \left(\boldsymbol{\mathcal{F}}_p^S \otimes \boldsymbol{e}_S\right) + \left(\boldsymbol{\mathcal{F}}_p^N \otimes \boldsymbol{e}_N\right). \tag{42}$$

In these expressions, the subscripts E, W, N, S refer to the edges of the domain, with the $\boldsymbol{e}$ vectors being equal to zero in every entry except for the first or last. The actual penalty vectors $\boldsymbol{\mathcal{F}}_{v_i}^W$ and $\boldsymbol{\mathcal{F}}_p^W$ are expressed as

$$\boldsymbol{\mathcal{F}}_{v_i}^W = \boldsymbol{H}_2 \boldsymbol{S}_{JW} \boldsymbol{n}_i^W \left(\boldsymbol{p}_W^* - \boldsymbol{p}_W\right), \qquad \boldsymbol{\mathcal{F}}_p^W = \boldsymbol{H}_2 \boldsymbol{S}_{JW} \lambda \left(\boldsymbol{v}_W^* - \boldsymbol{v}_W\right), \tag{43}$$

where the surface normals and Jacobians are given by

$$S_J = J \sqrt{\left(\frac{\partial \xi_i}{\partial x_2}\right)^2 + \left(\frac{\partial \xi_i}{\partial x_1}\right)^2}, \quad n_1 = \pm \frac{J}{S_J} \frac{\partial \xi_i}{\partial x_2}, \quad n_2 = \pm \frac{J}{S_J} \frac{\partial \xi_i}{\partial x_1}, \tag{44}$$

and the corresponding bolded matrices are constructed to be diagonal and contain values of these quantities at each grid point, as with $\boldsymbol{J}$ (see Eqn. (39)). The starred vectors $\boldsymbol{p}^*$ and $\boldsymbol{v}^*$ are specified by the boundary or interface condition.

It can be shown ([24], Appendix A) that the energy dissipation rate of an SBP block in this case is given by

$$\frac{dE}{dt} = \sum_{K=\{W,E,S,N\}} \mathcal{D}_K, \tag{45}$$

$$\mathcal{D}_K = -\boldsymbol{v}_K^T \boldsymbol{H}_K \boldsymbol{S}_{JK} \boldsymbol{p}_K^* + \boldsymbol{v}_K^T \boldsymbol{H}_K \boldsymbol{S}_{JK} \boldsymbol{p}_K - (\boldsymbol{v}_K^*)^T \boldsymbol{H}_K \boldsymbol{S}_{JK} \boldsymbol{p}_K. \tag{46}$$

Naturally, this dissipation rate, in conjunction with a definition of $\boldsymbol{p}^*$ and $\boldsymbol{v}^*$ based on the numerical characteristics of the interface, will be critical in proving stability via the energy method.

2.3.2 Discontinuous Galerkin Method

The discontinuous Galerkin method we will target our interface method(s) to will be briefly summarized here. As in Kozdon and Wilcox, we use a curvilinear triangle-based DG method, and we denote a DG element Ω_e with triangular reference element $\tilde{\Omega}$. To obtain a version of the governing equations (31)–(32) usable by DG, we must first obtain the variational form by introducing test functions w_i and φ for the velocities and pressure

respectively, multiplying them into their respective equations, and integrating over the reference element:

$$\int_{\tilde{\Omega}} w_i \left[\rho J \frac{\partial v_i}{\partial t} + \frac{\partial}{\partial \xi_1} \left(J \frac{\partial \xi_1}{\partial x_i} p \right) + \frac{\partial}{\partial \xi_2} \left(J \frac{\partial \xi_2}{\partial x_i} p \right) \right] dA$$

$$= - \int_{\partial \tilde{\Omega}} w_i S_J n_i \left(p^* - p \right) ds, \quad i = 1, 2, \tag{47}$$

$$\int_{\tilde{\Omega}} \varphi \left[J \frac{\partial p}{\partial t} + \lambda \left(J \frac{\partial \xi_1}{\partial x_1} \frac{\partial v_1}{\partial \xi_1} + J \frac{\partial \xi_2}{\partial x_1} \frac{\partial v_1}{\partial \xi_2} + J \frac{\partial \xi_1}{\partial x_2} \frac{\partial v_2}{\partial \xi_1} + J \frac{\partial \xi_2}{\partial x_2} \frac{\partial v_2}{\partial \xi_2} \right) \right] dA$$

$$= - \int_{\partial \tilde{\Omega}} \varphi \lambda S_J \left(v^* - v \right) ds, \tag{48}$$

In these equations, the normals n_i and surface Jacobians S_J are the same as the ones defined by Eqn. (44), and the starred quantities again refer to boundary and interface conditions implemented via penalization, in this instance better referred to as numerical fluxes. Applying integration by parts to Eqn. (47) to move the spatial derivatives to the test functions gives us the skew-symmetric form of the variational equations, which can then be spatially discretized with the DG method (see Hesthaven and Warburton [17] for more detail on this) to obtain:

$$\rho \boldsymbol{M}_J \frac{d\boldsymbol{v}_i}{dt} = \boldsymbol{D}_1^T \boldsymbol{M}_{1i} \boldsymbol{p} + \boldsymbol{D}_2^T \boldsymbol{M}_{2i} \boldsymbol{p} - \sum_{K=1}^{3} \boldsymbol{L}_K^T \boldsymbol{P}_{bc}^T \boldsymbol{n}_{iK} \boldsymbol{\Omega}_{bc} \boldsymbol{S}_{JK} \boldsymbol{p}_K^*, \tag{49}$$

$$\boldsymbol{M}_J \frac{d\boldsymbol{p}}{dt} = - \lambda \left(\boldsymbol{M}_{11} \boldsymbol{D}_1 \boldsymbol{v}_1 + \boldsymbol{M}_{21} \boldsymbol{D}_2 \boldsymbol{v}_1 + \boldsymbol{M}_{12} \boldsymbol{D}_1 \boldsymbol{v}_2 + \boldsymbol{M}_{22} \boldsymbol{D}_2 \boldsymbol{v}_2 \right)$$

$$- \sum_{K=1}^{3} \lambda \boldsymbol{L}_K^T \boldsymbol{P}_{bc}^T \boldsymbol{\Omega}_{bc} \boldsymbol{S}_{JK} \left(\boldsymbol{v}_K^* - \boldsymbol{v}_K^- \right). \tag{50}$$

These equations provide a semi-discretization on each element. The vector $\boldsymbol{v}_K^-$ is the normal component of velocity along edge K of the element evaluated at the cubature points:

$$\boldsymbol{v}_K^- = \boldsymbol{n}_{1K} P_{bc} \boldsymbol{L}_K \boldsymbol{v}_1 + \boldsymbol{n}_{2K} P_{bc} \boldsymbol{L}_K \boldsymbol{v}_2. \tag{51}$$

Edge-projected pressures are similarly defined as

$$\boldsymbol{p}_K^- = \boldsymbol{P}_{bc} \boldsymbol{L}_K \boldsymbol{p}. \tag{52}$$

In these expressions, $\boldsymbol{L}_K$ and $\boldsymbol{L}_K^T$ are operators which take volume terms to edge K of the element and edge K terms to the volume respectively. $\boldsymbol{D}_1$ and $\boldsymbol{D}_2$ are the reference element differentiation matrices for the two reference coordinate directions. The projection matrices $\boldsymbol{P}_c$ and $\boldsymbol{P}_{bc}$ project from the volume and edge approximations to the volume and edge cubature points, respectively. The matrices $\boldsymbol{\Omega}_c$ and $\boldsymbol{\Omega}_{bc}$ are diagonal matrices of the integration weights for the volume and an edge, respectively, defined at the cubature locations. A critical condition assumed by [24] for stability of their method is that $\boldsymbol{\Omega}_c$ and $\boldsymbol{\Omega}_{bc}$ are positive definite. Finally, the element mass matrices in the discretization are defined as

$$\boldsymbol{M}_J = P_c^T \boldsymbol{\Omega}_c J P_c, \quad \boldsymbol{M}_{ij} = P_c^T \boldsymbol{\Omega}_c J \frac{\partial \xi_i}{\partial x_j} P_c. \tag{53}$$

Here the diagonal matrices $\boldsymbol{J}$ and $\frac{\partial \boldsymbol{\xi_i}}{\partial \boldsymbol{x_j}}$ are defined identically to Eqn. (39) and defined at the cubature points. The diagonal matrices $\boldsymbol{S}_{JK}$ and $\boldsymbol{n}_{iK}$ are defined in the same way at the cubature points.

As with SBP, it can be shown that a single DG element has the energy dissipation rate

$$\frac{dE}{dt} = \sum_{K=1}^{3} \mathcal{D}_K, \tag{54}$$

$$\mathcal{D}_K = - \left(\boldsymbol{v}_K^- \right)^T \boldsymbol{\Omega}_{bc} \boldsymbol{S}_{JK} \boldsymbol{p}_K^* - \left(\boldsymbol{p}_K^- \right)^T \boldsymbol{\Omega}_{bc} \boldsymbol{S}_{JK} \left(\boldsymbol{v}_K^* - \boldsymbol{v}_K^- \right). \tag{55}$$

As in the case of SBP, this relation is naturally critical in establishing the energy stability of the interface, especially considering its direct incorporation of starred (interface-driven) quantities.

2.3.3 Interface Method

Clearly vital in the proof of energy stability for the marriage of the above methods is the definition of the terms $\boldsymbol{p}^*$ and $\boldsymbol{v}^*$, most often referred to as the numerical fluxes (in the context of DG) or penalty terms (in the context of SBP-SAT). At the interface between the two discretizations, these quantities are naturally contingent on the nature of the interface method, which for the purpose of this discussion take a basic form based on projection operators that move the Grid a solutions to Grid b,

$$\boldsymbol{f}_a = \boldsymbol{P}_{b2a} \boldsymbol{f}_b \tag{56}$$

$$\boldsymbol{f}_b = \boldsymbol{P}_{a2b} \boldsymbol{f}_a, \tag{57}$$

where f_a is of course a function defined on Grid a and f_b is a function defined on Grid b. Note that it is nowhere stated (and in fact proves to be untrue for SBP-to-SBP projection using Kozdon and Wilcox's method) that $\boldsymbol{P}_{a2b} \boldsymbol{P}_{b2a} = \boldsymbol{I}$.

To discuss the construction of the projection operation itself, we use the work of Kozdon and Wilcox as a starting point. As detailed in their paper, their operators rely primarily upon the principle of projecting solutions from either discretization first into an intermediate "glue" space of piecewise continuous polynomials before projecting the solution onto the other nonconforming discretization. Whereas the solution on the respective structured and unstructured grids is represented at the block boundaries on the grid points, the solution on the intermediate glue grid is represented on each interval by modal coefficient values multiplying Legendre polynomials defined on the interval $[-1, 1]$.

The critical condition that allows proof of stability is referred to as the *compatibility condition*, and amounts to a simple relation between the grid-to-glue and glue-to-grid projection operators, the mass matrix of the piecewise polynomial description used in the glue layer, and a norm operator $\boldsymbol{H}$:

$$\boldsymbol{P}_{f2g} \boldsymbol{M} = \boldsymbol{P}_{g2f}^T \boldsymbol{H} \tag{58}$$
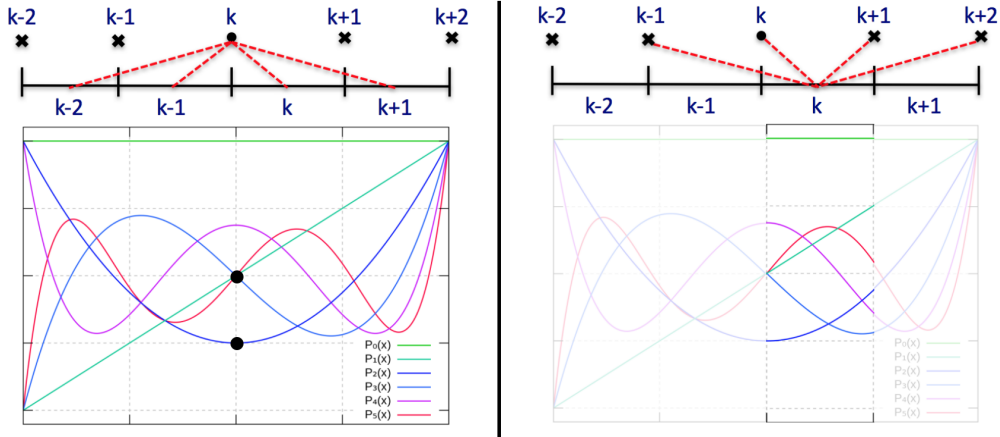
Figure 6: Images demonstrating the interior constraints for the projection mimicking SBP4-2 operators. Left: projection of modal coefficients of the piecewise polynomial solution on the four surrounding glue grid intervals to the central grid point in the stencil must result in a correct Legendre polynomial solution at point k up to the interior order. Right: projection of the solutions at the four points surrounding interval k to the modal coefficients on interval k must produce the correct piecewise approximation of Legendre polynomials up to interior order on that interval.

In the case of SBP finite difference discretizations, the norm $\boldsymbol{H}$ is equivalent to the SBP-norm, which, for the purpose of this work, we will take to be a diagonal matrix. In the case of discontinuous Galerkin, the $\boldsymbol{H}$ operator is the diagonal matrix of integration weights at the cubature points at a single DG element edge, $\boldsymbol{\Omega}_{bc}$. This compatibility condition, used in conjunction with the per-block semi-discrete expressions for energy dissipation (Eqn. (46) and (55)) and a careful defintion of the interface quantities themselves, is what allows for energy stability to be proven.

Given its clear importance, the compatibility condition (Eqn. (58)) is used as an explicit constraint when constructing the projection operators $\boldsymbol{P}_{f2g}$ and $\boldsymbol{P}_{g2f}$ themselves. The construction, which is laid out in further detail in [24] (Appendix B), defines interior and boundary accuracy conditions when projecting from grid to glue (and vice versa) that match those of corresponding SBP diagonal-norm operators of the same order. A pictorial representation of this process is given by Figure 6. These conditions, in conjunction with symmetry conditions, result in a *non-square* system featuring more unknowns than constraints, in particular near the boundary stencils. Given the underdetermined nature of the system, the authors then use an optimization procedure aimed at minimizing the distance between the nearest eigenvalues of $\boldsymbol{B} = \boldsymbol{P}_{f2g}\boldsymbol{P}_{g2f}$ to produce the final projection operators for a given order.

Equally critical to the construction of the projection operators is how they are used to describe the penalty terms and numerical fluxes in the respective discretizations. The conditions enforced at the interface for the governing equations (31)–(32) are continuity of both pressure and velocity normal to the interface; that is,

$$\boldsymbol{p}^+ = \boldsymbol{p}^- \qquad \boldsymbol{v}^+ = -\boldsymbol{v}^-, \tag{59}$$

where we describe the quantities on either side of the interface using + and – superscripts. Using a *conforming* interface as a stepping stone, the interfacial terms $\boldsymbol{p}^*$ and $\boldsymbol{v}^*$ in the energy dissipation relations (Eqn. (46) for SBP blocks and Eqn. (55) for DG) can be obtained from

$$\boldsymbol{p}^* - \boldsymbol{p} = \boldsymbol{p}^* - \boldsymbol{p}^- = \frac{1}{2}\left(\boldsymbol{p}^+ - \boldsymbol{p}^-\right) + \alpha\frac{Z}{2}\left(\boldsymbol{v}^+ + \boldsymbol{v}^-\right), \tag{60}$$

$$\boldsymbol{v}^* - \boldsymbol{v} = \boldsymbol{v}^* - \boldsymbol{v}^- = -\frac{1}{2}\left(\boldsymbol{v}^+ + \boldsymbol{v}^-\right) - \alpha\frac{1}{2Z}\left(\boldsymbol{p}^+ - \boldsymbol{p}^-\right), \tag{61}$$

where α controls the upwind nature of the penalization ($\alpha = 1$ gives an upwind penalty, whereas $\alpha = 0$ gives a central penalty), and the impedance is given by $Z = \sqrt{\rho/\lambda}$. For *nonconforming* interfaces like the one we are constructing, we will employ this same relation to define glue-grid quantities $\bar{\boldsymbol{p}}^*$ and $\bar{\boldsymbol{v}}^*$, given that the discretizations *conform at the glue grid interval level*. Furthermore, we can define the + and – quantities on the glue grid using the projection operators on either side of the interface

$$\bar{\boldsymbol{v}}^{\pm} = \boldsymbol{P}^{\pm}_{f2g}\left(\frac{\boldsymbol{S}^{\pm}_J}{\Delta^{\pm}}\right)^{1/2}\boldsymbol{v}^{\pm}, \tag{62}$$

$$\bar{\boldsymbol{p}}^{\pm} = \boldsymbol{P}^{\pm}_{f2g}\left(\frac{\boldsymbol{S}^{\pm}_J}{\Delta^{\pm}}\right)^{1/2}\boldsymbol{p}^{\pm}, \tag{63}$$

noting that projection of the surface Jacobian at the interface is also required. Note also the inclusion of a factor $\Delta^{\pm}$ scaling the surface Jacobian — this factor accounts for the fact that each DG element is treated as a separate block and only intersects the glue grid in a small interval (for the SBP-side of the interface, Δ is unity unless multiple separate SBP blocks intersect with the interface). From here, we can write the SAT penalty terms along the interface (assuming the SBP-SAT discretization to form the – side of the interface, and assuming a single SBP block) as a function of purely glue grid defined quantities:

$$\boldsymbol{p}^* - \boldsymbol{p}^- = \left(\boldsymbol{S}^-_J\right)^{-1/2}\boldsymbol{P}^-_{g2f}\left(\bar{\boldsymbol{p}}^* - \bar{\boldsymbol{p}}^-\right) + \frac{1}{2}\left[\left(\boldsymbol{S}^-_J\right)^{-1/2}\boldsymbol{P}^-_{g2f}\bar{\boldsymbol{p}}^- - \boldsymbol{p}^-\right], \tag{64}$$

$$\boldsymbol{v}^* - \boldsymbol{v}^- = \left(\boldsymbol{S}^-_J\right)^{-1/2}\boldsymbol{P}^-_{g2f}\left(\bar{\boldsymbol{v}}^* - \bar{\boldsymbol{v}}^-\right) + \frac{1}{2}\left[\left(\boldsymbol{S}^-_J\right)^{-1/2}\boldsymbol{P}^-_{g2f}\bar{\boldsymbol{v}}^- - \boldsymbol{v}^-\right], \tag{65}$$

where $\bar{\boldsymbol{p}}^* - \bar{\boldsymbol{p}}^-$ and $\bar{\boldsymbol{v}}^* - \bar{\boldsymbol{v}}^-$ are defined by Eqn. (60)–(61) using the values $\bar{\boldsymbol{p}}^{\pm}$ and $\bar{\boldsymbol{v}}^{\pm}$ for $\boldsymbol{p}^{\pm}$ and $\boldsymbol{v}^{\pm}$, respectively. The second term in each equation is described by [24] as a projection error, but also proves to be crucial in the ensuing energy stability proof.

As for discontinuous Galerkin, the numerical flux is similarly given by

$$\boldsymbol{p}^* = \left(\frac{\boldsymbol{S}^+_J}{\Delta^+}\right)^{-1/2}\boldsymbol{P}^+_{g2f}\bar{\boldsymbol{p}}^*, \tag{66}$$

$$\boldsymbol{v}^* - \boldsymbol{v}^+ = \left(\frac{\boldsymbol{S}^+_J}{\Delta^+}\right)^{-1/2}\boldsymbol{P}^+_{g2f}\left(\bar{\boldsymbol{v}}^* - \bar{\boldsymbol{v}}^+\right). \tag{67}$$

Note that this expression amounts to the same expression as given for the SAT penalty terms, but for the opposite side of the interface, including the element-to-interface scaling

factor, and with no projection error included as in the case of SAT. These definitions of numerical fluxes and penalty terms for the two discretizations, as shown in [24], yield an energy-stable interface.

As mentioned in Section 2.1, our goal is to eliminate the optimization procedure incorporated into the construction of the projection operators, either by imposing more constraints (such as steps towards round-trip projection fidelity) or removing extraneous unknowns. The implication of the underdetermined system, in other words, is that we can *ask for more*.

2.4 Validation Plan

The test problem for validation will match that of [24], modeling the two-dimensional acoustic wave equation in first-order form with the following initial condition:

$$p(x_1, x_2, 0) = \cos\left(k_1 x_1\right) \cos\left(k_1 x_2\right) + \sin\left(k_2 x_1\right) \sin\left(k_2 x_2\right), \tag{68}$$

$$v_i(x_1, x_2, 0) = 0, \qquad i = 1, 2, \tag{69}$$

where $k_1 = \pi/2$ and $k_2 = \pi$. All exterior boundary conditions are zero pressure (free-surface) conditions. The exact solution of this problem is

$$p(x_1, x_2, t) = \cos\left(\omega_1 t\right) \cos\left(k_1 x_1\right) \cos\left(k_1 x_2\right) + \cos\left(\omega_2 t\right) \sin\left(k_2 x_1\right) \sin\left(k_2 x_2\right), \tag{70}$$

$$v_1(x_1, x_2, t) = \frac{k_1}{\omega_1} \sin\left(\omega_1 t\right) \sin\left(k_1 x_1\right) \cos\left(k_1 x_2\right) - \frac{k_2}{\omega_2} \sin\left(\omega_2 t\right) \cos\left(k_2 x_1\right) \sin\left(k_2 x_2\right), \tag{71}$$

$$v_2(x_1, x_2, t) = \frac{k_1}{\omega_1} \sin\left(\omega_1 t\right) \cos\left(k_1 x_1\right) \sin\left(k_1 x_2\right) - \frac{k_2}{\omega_2} \sin\left(\omega_2 t\right) \sin\left(k_2 x_1\right) \cos\left(k_2 x_2\right), \tag{72}$$

where $\omega_j = k_j \sqrt{2}$ for $j = 1, 2$.

As for the spatial discretization, we will employ a square spatial domain with the left half using diagonal-norm SBP operators for finite differencing, and the right half using a discontinuous Galerkin method (see Figure 7). The interior order of the SBP method, as well as the order of the projection across the interface, is specified to match the order of the discontinous Galerkin method. Our success metrics for this test problem include:

- Demonstrating accurate recreation of the total energy of the system, as observed in the numerical simulation of the problem, via a comparison of the total energy calculated from the time-integrated state and the total energy calculated via time-integration of a dissipation rate derived from the spatial and interfacial schema.

- Demonstrating that this energy does not increase (condition for semi-discrete stability).

- Demonstrating the prescribed order of accuracy using L^2 norms.

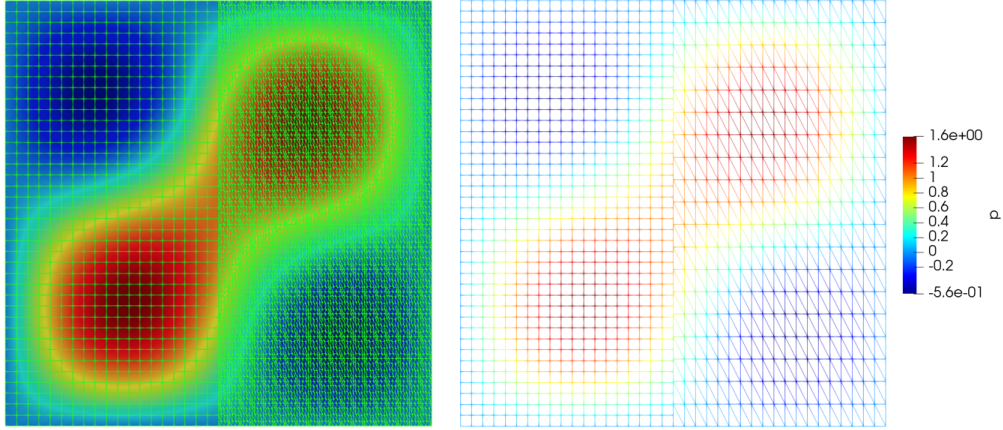Upon fulfillment of these goals, extension to three dimensions will be considered.

Figure 7: Pressure initial condition for test problem, also showing split-domain discretization. The right figure coarsens the wireframe to better show the individual triangular DG elements.

2.5 Outlook

2.5.1 Current Status

Current work on this project has thus far amounted to reconstruction of the operators of Kozdon and Wilcox, application of these operators to simple, periodic SBP-to-SBP advection examples, and verification of their accuracy and energy-stability properties when focusing on the use of the interior projection stencil (see Figure 8). Having both verified and better understood the construction and capabilities of these operators, the question then becomes improving upon them, and the chief task to that end is better understanding the importance of the compatibility condition in both the construction of the operators and in the proof of energy stability. Namely, a question being asked via the use of symbolic evaluation tools such as Maxima [26] is whether there are alternative conditions on the grid-to-glue projection that will provide similar characteristics. In particular, one question that demands answer pertains directly to the *interior* operator construction, which in the grid-to-glue direction amounts to an equal number of degrees of freedom and accuracy constraints imposed upon the glue grid intervals (see Figure 6). In this case, the projection in the glue-to-grid direction can then be fully determined by the compatibility condition (Eqn. (58)), but it is not clear why this also results in a glue-to-grid projection operator that fulfills its own accuracy constraints imposed on the grid points.

Additionally, and related to these questions, another avenue of investigation is in the choices of the degree-of-freedom pattern in the projection from grid to glue layer and vice versa, as well as whether or not there are other polynomial bases for the glue layer that maintain positive-definite mass matrices while also introducing improved accuracy. Finally, the compatibility condition itself, and namely whether or not there are other conditions on the projection operators that may fulfill similar goals, may be called into question.
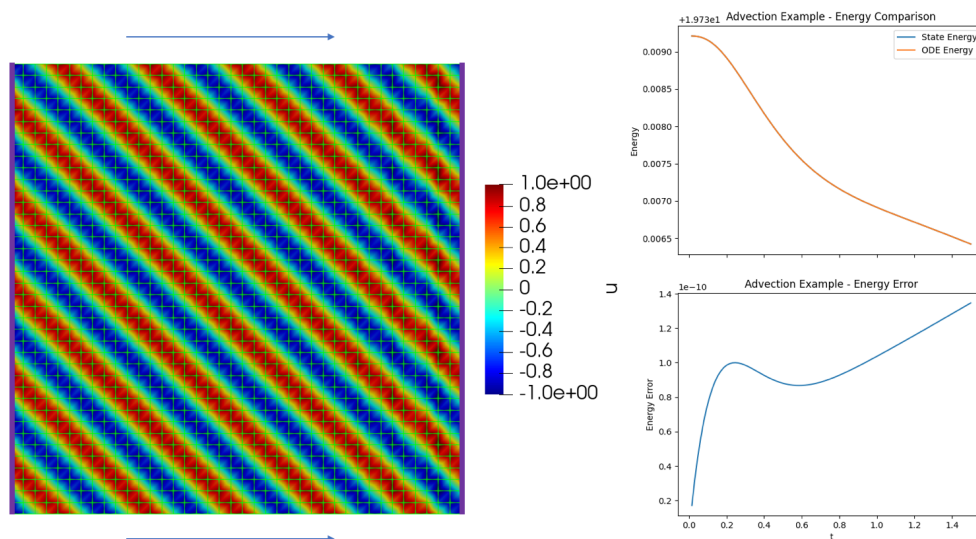
Figure 8: Application of the glue layer projection theory of [24] to a scalar advection example with an advection speed of 1. The purple line in the figure on the left is a glue layer to which we project the solution on the rightmost grid points at the periodic boundary in x. We then project from the glue layer to the leftmost set of grid points. The plots on the right show both an overall decrease in energy (energy stability) and a good agreement between the energy calculated from the time-integrated state and the energy calculated from time-integrating the energy dissipation rate.

2.5.2 Risk Mitigation

Should our goal of a new and unisolvent stable interface method not come to fruition, a "fallback" goal of sorts is identified in that Kozdon and Wilcox's method has yet to be extended to three dimensions. This would likely present more of a technical challenge than an theoretical one, but a study of how the method responds to certain geometric scenarios untestable in two dimensions (namely three-dimensional corners) has potential to yield further information about how the optimized operators perform numerically, as well as shed light on optimization targets to yield better results in higher dimensions.

Furthermore, an additional unexplored topic that could prove to be a worthwhile "fallback" goal — and one that potentially ties the two topics of this proposal together — would be exploring the implications of the use of Kozdon and Wilcox's projection operators on the timestep limitations of a given physical problem, and (if a timestep disparity between the interior of a given subdomain and its interface with another subdomain is identified) exposing this challenge to multi-rate Adams integration.

References

[1] Martin Almquist, Siyang Wang, and Jonatan Werpers. Order-preserving interpolation for summation-by-parts operators at nonconforming grid interfaces. *SIAM Journal on*

Scientific Computing, 41(2):A1201–A1227, 2019.

[2] Uri M Ascher and Linda R Petzold. *Computer methods for ordinary differential equations and differential-algebraic equations*, volume 61. Siam, 1998.

[3] Francis Bashforth and John Couch Adams. *An attempt to test the theories of capillary action*. University Press, 1883.

[4] William Blumen. Shear layer instability of an inviscid compressible fluid. *Journal of Fluid Mechanics*, 40(4):769–781, 1970.

[5] Daniel J Bodony. Accuracy of the simultaneous-approximation-term boundary condition for time-dependent problems. *Journal of Scientific Computing*, 43(1):118–133, 2010.

[6] Daniel J Bodony, George Zagaris, Adam Reichert, and Qi Zhang. Provably stable overset grid methods for computational aeroacoustics. *Journal of Sound and Vibration*, 330(17):4161–4179, 2011.

[7] Mark H Carpenter, David Gottlieb, and Saul Abarbanel. Time-stable boundary conditions for finite-difference schemes solving hyperbolic systems: methodology and application to high-order compact schemes. Technical report, NASA, 1993.

[8] Scott D Cohen, Alan C Hindmarsh, and Paul F Dubois. Cvode, a stiff/nonstiff ode solver in c. *Computers in physics*, 10(2):138–143, 1996.

[9] Emil M Constantinescu and Adrian Sandu. Multirate timestepping methods for hyperbolic conservation laws. *Journal of Scientific Computing*, 33(3):239–278, 2007.

[10] Emil M Constantinescu and Adrian Sandu. Extrapolated implicit-explicit time stepping. *SIAM Journal on Scientific Computing*, 31(6):4452–4477, 2010.

[11] Emil M Constantinescu and Adrian Sandu. Extrapolated multirate methods for differential equations with multiple time scales. *Journal of Scientific Computing*, 56(1):28–44, 2013.

[12] Nicholas J Curtis, Kyle E Niemeyer, and Chih-Jen Sung. Using simd and simt vectorization to evaluate sparse chemical kinetic jacobian matrices and thermochemical source terms. *Combustion and Flame*, 198:186–204, 2018.

[13] Lucas Friedrich, David C Del Rey Fernández, Andrew R Winters, Gregor J Gassner, David W Zingg, and Jason Hicken. Conservative and stable degree preserving sbp operators for non-conforming meshes. *Journal of Scientific Computing*, 75(2):657–686, 2018.

[14] Longfei Gao, Omar Ghattas, and David Keyes. Energy-conserving 3d elastic wave simulation with finite difference discretization on staggered grids with nonconforming interfaces. *arXiv preprint arXiv:2012.13863*, 2020.

[15] Charles William Gear and DR Wells. Multirate linear multistep methods. *BIT Numerical Mathematics*, 24(4):484–502, 1984.

[16] David G. Goodwin, Raymond L. Speth, Harry K. Moffat, and Bryan W. Weber.

Cantera: An object-oriented software toolkit for chemical kinetics, thermodynamics, and transport processes. `https://www.cantera.org`, 2018. Version 2.4.0.

[17] Jan S Hesthaven and Tim Warburton. *Nodal discontinuous Galerkin methods: algorithms, analysis, and applications.* Springer Science & Business Media, 2007.

[18] Patrick Hin Fun Hung. *Algorithms for reaction mechanism reduction and numerical simulation of detonations initiated by projectiles.* PhD thesis, California Institute of Technology, 2003.

[19] Christopher A Kennedy and Mark H Carpenter. Additive runge–kutta schemes for convection–diffusion–reaction equations. *Applied numerical mathematics*, 44(1-2):139–181, 2003.

[20] A. Klöckner and M. Wala. Dagrt. `https://github.com/inducer/dagrt`, 2020.

[21] A. Klöckner and M. Wala. Leap. `https://github.com/inducer/leap`, 2020.

[22] Andreas Klöckner. *High-performance high-order simulation of wave and plasma phenomena.* PhD thesis, Brown University, 2010.

[23] Omar M Knio, Habib N Najm, and Peter S Wyckoff. A semi-implicit numerical scheme for reacting flow: Ii. stiff, operator-split formulation. *Journal of Computational Physics*, 154(2):428–467, 1999.

[24] Jeremy E Kozdon and Lucas C Wilcox. Stable coupling of nonconforming, high-order finite difference methods. *SIAM Journal on Scientific Computing*, 38(2):A923–A952, 2016.

[25] Simon Lapointe, Sudeepta Mondal, and Russell A Whitesides. Data-driven selection of stiff chemistry ode solver in operator-splitting schemes. *Combustion and Flame*, 220:133–143, 2020.

[26] Jinhu Li and Jeffrey S Racine. Maxima: An open source computer algebra system, 2008.

[27] Tomas Lundquist, Arnaud Malan, and Jan Nordström. A hybrid framework for coupling arbitrary summation-by-parts schemes on general meshes. *Journal of Computational Physics*, 362:49–68, 2018.

[28] Tomas Lundquist and Jan Nordström. On the suboptimal accuracy of summation-by-parts schemes with non-conforming block interfaces, 2016.

[29] Jonathan F MacArt and Michael E Mueller. Semi-implicit iterative methods for low mach number turbulent reacting flows: Operator splitting versus approximate factorization. *Journal of Computational Physics*, 326:569–595, 2016.

[30] Ken Mattsson and Mark H Carpenter. Stable and accurate interpolation operators for high-order multiblock finite difference methods. *SIAM Journal on Scientific Computing*, 32(4):2298–2320, 2010.

[31] Ken Mattsson, Magnus Svärd, and Jan Nordström. Stable and accurate artificial dissipation. *Journal of Scientific Computing*, 21(1):57–79, 2004.

[32] Bonnie J McBride. *NASA Glenn coefficients for calculating thermodynamic properties of individual species*. National Aeronautics and Space Administration, John H. Glenn Research Center ..., 2002.

[33] Alfons Michalke. On the inviscid instability of the hyperbolictangent velocity profile. *Journal of Fluid Mechanics*, 19(4):543–556, 1964.

[34] Cory Mikida, Andreas Klöckner, and Daniel Bodony. Multi-rate time integration on overset meshes. *Journal of Computational Physics*, 396:325–346, 2019.

[35] Forest Ray Moulton. *New methods in exterior ballistics*. Chicago, 1926.

[36] Anna Nissen, Katharina Kormann, Magnus Grandin, and Kristoffer Virta. Stable difference methods for block-oriented adaptive grids. *Journal of Scientific Computing*, 65(2):486–511, 2015.

[37] Anna Nissen, Gunilla Kreiss, and Margot Gerritsen. Stability at nonconforming grid interfaces for a high order discretization of the schrödinger equation. *Journal of Scientific Computing*, 53(3):528–551, 2012.

[38] Ralph Noack and Jeffrey Slotnick. A summary of the 2004 overset symposium on composite grids and solution technology. In *43rd AIAA Aerospace Sciences Meeting and Exhibit*, page 921, 2005.

[39] Jan Nordström and Jing Gong. A stable hybrid method for hyperbolic problems. *Journal of Computational Physics*, 212(2):436–453, 2006.

[40] Zhuyin Ren and Stephen B Pope. Second-order splitting schemes for a class of reactive systems. *Journal of Computational Physics*, 227(17):8165–8176, 2008.

[41] Bruno Sportisse, Guy Bencteux, and Pierre Plion. Method of lines versus operator splitting for reaction–diffusiuon systems with fast chemistry. *Environmental Modelling & Software*, 15(6-7):673–679, 2000.

[42] Bo Strand. Summation by parts for finite difference approximations for d/dx. *Journal of Computational Physics*, 110(1):47–67, 1994.

[43] Gilbert Strang. On the construction and comparison of difference schemes. *SIAM journal on numerical analysis*, 5(3):506–517, 1968.

[44] Magnus Svärd, Mark H Carpenter, and Jan Nordström. A stable high-order finite difference scheme for the compressible Navier–Stokes equations, far-field boundary conditions. *Journal of Computational Physics*, 225(1):1020–1038, 2007.

[45] Magnus Svärd and Siddhartha Mishra. Implicit–explicit schemes for flow equations with stiff source terms. *Journal of computational and applied mathematics*, 235(6):1564–1577, 2011.

[46] Magnus Svärd and Jan Nordström. A stable high-order finite difference scheme for the compressible Navier–Stokes equations: no-slip wall boundary conditions. *Journal of Computational Physics*, 227(10):4805–4824, 2008.

[47] Siyang Wang, Kristoffer Virta, and Gunilla Kreiss. High order finite difference meth-

ods for the wave equation with non-conforming grid interfaces. *Journal of Scientific Computing*, 68(3):1002–1028, 2016.

[48] San Diego Mechanism web page. Chemical-kinetic mechanisms for combustion applications.

[49] Bao Zhu, Jiefu Chen, Wanxie Zhong, and Qing Huo Liu. A hybrid fetd-fdtd method with nonconforming meshes. *Communications in Computational Physics*, 9(3):828–842, 2011.